Biomaterials Science

ROYAL SOCIETY OF CHEMISTRY

PAPER

View Article Online
View Journal | View Issue

Cite this: *Biomater. Sci.*, 2025, **13**, 6378

Charge modulation in D–A–D molecules: an acid-responsive NIR-II nanoplatform for imaging and phototherapy

Shu Gao,[a,c] Jiahui Wang,[d] Xiaonan Wei,[a,e] Jun Wang,[a,c] Yuanpeng Jiang,[a,c] Boyu Tan,[a,f] Yeshan Qin,[a] Xiaoyang Zhu,[g] Ruihu Song,[a] Chunrong Qu,*[a] Kun Qian*[a] and Zhen Cheng *[a,b,c]

Small-molecule near-infrared (NIR) dyes have shown great promise in bioimaging and theranostics of diseases. Among them, D–A–D-structured molecules stand out because of their excellent photostability, second near-infrared window (NIR-II, 1000–2000 nm) emission, and large Stokes shifts, offering significant imaging advantages and application potential. However, compared to conventional BODIPY and cyanine-based dyes, D–A–D molecules are generally uncharged and exhibit poor solubility, which limit their further application in biological systems. To date, systematic studies on the photophysical properties of charged D–A–D molecules have remained scarce. Considering the importance of structural modulation, a detailed investigation of their optical properties is of great significance for rational design of practical and high-performance dyes. In this study, two groups of D–A–D-type small-molecule dyes were rationally designed and synthesized based on a donor–acceptor engineering strategy. The influence of charge incorporation on their photophysical properties was systematically evaluated. Among them, SMIC-10004 exhibited excellent optical stability, good polarity, and favorable NIR-II emission characteristics. Based on this, an acid-responsive nanoprobe, SMIC-10004 NPs, was constructed using mPEG-Hyd-DSPE to enhance accumulation in the tumor microenvironment. *In vivo* experiments demonstrated that SMIC-10004 NPs enabled high-resolution and long-term NIR-II imaging, and the nanoparticles significantly inhibited tumor growth under laser irradiation, showing superior photothermal therapeutic efficacy with good biocompatibility. Overall, this study not only provides valuable guidance for the rational design of charged D–A–D dyes, but also presents a promising platform for NIR-II-based theranostic applications.

Received 16th July 2025,
Accepted 17th September 2025

DOI: 10.1039/d5bm01084e

rsc.li/biomaterials-science

1. Introduction

The second near-infrared window (NIR-II, 1000–2000 nm) outperforms the visible and NIR-I windows for *in vivo* fluorescence imaging by minimizing scattering and autofluorescence, enabling deep, high-contrast, real-time imaging with strong clinical promise.[1–3] Although numerous NIR-II imaging probes based on inorganic materials—such as semiconducting polymers and quantum dots—exhibit excellent photophysical properties,[4–6] concerns regarding slow clearance, heavy metal leakage, and long-term toxicity hinder their clinical translation.[7] In contrast, small-molecule dyes offer favorable biocompatibility because of their biodegradability, rapid clearance, and low toxicity.[8] Furthermore, their tunable structures enable systematic molecular engineering to optimize NIR-II fluorescence performance for specific imaging needs.

Phototheranostics offers advantages such as non-invasiveness, convenience, and low risk[9] and has emerged as a research hotspot in recent years. The performance of near-infrared photothermal agents and photosensitizers largely determines the therapeutic outcomes.[10,11] Therefore, the development of next-generation near-infrared dyes is of great significance for advancing phototheranostics. Common NIR fluo-

[a]*State Key Laboratory of Drug Research, Molecular Imaging Center, Shanghai Institute of Materia Medica, Chinese Academy of Sciences, Shanghai, 201203, China. E-mail: crqu@simm.ac.cn*
[b]*Shandong Laboratory of Yantai Drug Discovery, Bohai Rim Advanced Research Institute for Drug Discovery, Yantai, Shandong 264117, China. E-mail: zcheng@simm.ac.cn*
[c]*School of Pharmacy, University of Chinese Academy of Sciences, No.19A Yuquan Road, Beijing 100049, China*
[d]*Tianjin University of Traditional Chinese Medicine, Tianjin 301617, China*
[e]*Shandong First Medical University & Shandong Academy of Medical Sciences, Huaiyin District, No.6699, Qingdao Road, Jinan, 250000 Shandong, China*
[f]*School of Biomedical Engineering, ShanghaiTech University, Shanghai 201210, China*
[g]*School of Chinese Materia Medica, Nanjing University of Chinese Medicine, Nanjing 210023, China*

rescent small-molecule scaffolds include cyanines, rhodamines, diketopyrrolopyrroles, BODIPYs, squaraines, and donor–acceptor–donor (D–A–D) systems.[12–15] Among them, D–A–D dyes possess excellent photostability and large Stokes shifts.[16] One of the key features of D–A–D architectures is the use of rigid, strongly electron-deficient acceptor cores to facilitate efficient charge transfer. Benzo[1,2-*c*:4,5-*c*′]bis([1,2,5]thiadiazole) (BBTD) is one of the most classical electron acceptors, well known for its strong electron-withdrawing capability.[17] Notably, the first reported NIR-II dye, CH1055, was constructed based on the BBTD core.[18] However, its synthesis can be challenging. In comparison, the 6,7-diphenyl-[1,2,5]thiadiazolo[3,4-*g*]quinoxaline (TQX) core features lower synthetic complexity and greater chemical stability,[19] making it a promising alternative for imaging and photothermal therapy. To date, numerous NIR-II probes have been designed and used in the diagnosis and treatment of various diseases.[20–22] NIR-triggered theranostic agents have already demonstrated great potential for treating deep-seated diseases.[23,24] Several studies have examined dye design and performance enhancement from structural and aggregation perspectives.[25,26] However, comprehensive studies on the physicochemical properties of D–A–D dyes remain limited.

Incorporating charged moieties not only enhances intramolecular charge transfer and modulates absorption and emission profiles, but also increases molecular polarity and dispersibility in aqueous environments, thereby improving the biocompatibility and biological application feasibility.[27,28] Previous studies showed that the negatively charged intracellular environment attracts positively charged molecules,[29] and cationic groups facilitate subcellular targeting, as seen in mitochondria-targeting probes with lipophilic cationic structures.[30] Recently, cationic groups like quaternary ammonium and pyridinium have been incorporated into donor or acceptor units to enhance the dye performance,[31] but most studies remain limited to the visible or NIR-I region. Currently, cationic NIR-II probes are mainly limited to cyanine, BODIPY, and rhodamine derivatives, whereas cationic D–A–D-type molecules have rarely been reported. Systematic studies on the influence of charge position and density on NIR-II dye properties remain scarce. Quaternized pyridine forms a stable pyridinium ion under physiological conditions and serves as a conjugated unit in D–A–D structures, making it a useful scaffold for designing positively charged NIR-II probes and studying structure–property relationships in biomedical imaging and therapy.

In this study, based on BBTD and TQX scaffolds, we thus employed a donor–acceptor engineering strategy to construct two groups of neutral and positively charged D–A–D molecules, aiming to investigate the impact of cationic modification on their photophysical properties and theranostic potential. These molecules maintain high structural rigidity and extended π-conjugation. With similar donors, TQX exhibits red-shifted absorption and emission and higher photothermal conversion efficiency compared with BBTD, indicating its promise as a photothermal agent. Compared with some currently available theranostic agents, SMIC dyes exhibit better photostability, larger Stokes shifts, and broader emission bandwidths, which are conducive to improving the theranostic performance. Meanwhile, the incorporation of charged groups could enhance their solubility in aqueous media. This approach holds promise for guiding the rational design of next-generation dyes with superior performance and tailored biological functionalities. To further evaluate their *in vivo* applications, D–A–D dyes were encapsulated using mPEG-Hyd-DSPE, enabling prolonged blood circulation and pH-responsive behavior in acidic environments. This strategy enhances tumor accumulation and ultimately yields a theranostic agent capable of long-term imaging *in vivo*.

2. Results and discussion

2.1. Design, synthesis, and characterization of cationic D–A–D fluorescent probes

The introduction of pyridine moieties expands the π-conjugation framework and provides a modifiable nitrogen atom bearing a lone pair of electrons. Upon methylation, the resulting *N*-methylpyridinium salt introduces a positive charge and acts as a strong electron-withdrawing group. Additionally, π-bridges serve as effective structural elements to further extend conjugation. Alkyl-substituted thiophenes were incorporated to enhance lipophilicity and protect the excited-state core *via* hydrophobic interactions, thereby reducing susceptibility to external electrophilic attacks by polar solvent molecules and simplifying purification during synthesis. A total of four D–A–D-type small molecules—SMIC-10001, SMIC-10002, SMIC-10003, and SMIC-10004—were successfully synthesized through Stille coupling and SN2 nucleophilic substitution reactions. These molecules were designed to investigate the impact of various electron-accepting groups on optical properties (Fig. 1a). Among them, the optimally selected SMIC-10004 was encapsulated into mPEG-Hyd-DSPE to form organic nanoparticles for NIR-II fluorescence imaging and photothermal therapy (Fig. 1b). The successful synthesis of target compounds was confirmed by matrix-assisted laser desorption/ionization time-of-flight mass spectrometry (MALDI-TOF MS) and nuclear magnetic resonance (NMR) spectroscopy, including both ^{1}H NMR and ^{13}C NMR (Fig. S1–14). Detailed synthetic procedures and characterization data are provided in the SI.

The normalized absorption and emission spectra of the synthesized compounds were recorded in dichloromethane (DCM). As shown in the spectra (Fig. 1c). SMIC-10001 exhibited a maximum absorption at 664 nm. Owing to the strong electron-accepting ability of the BBTD core, its emission spectrum extended beyond 1000 nm. Methylation of SMIC-10001 yielded the cationic analogue SMIC-10002, which displayed hypsochromic shifts of 23 nm and 25 nm in absorption and emission maxima, respectively, while maintaining a comparable Stokes shift. In parallel, SMIC-10002 showed markedly improved solubility in polar solvents. Whereas SMIC-10001 was readily soluble in DCM but poorly soluble in methanol,

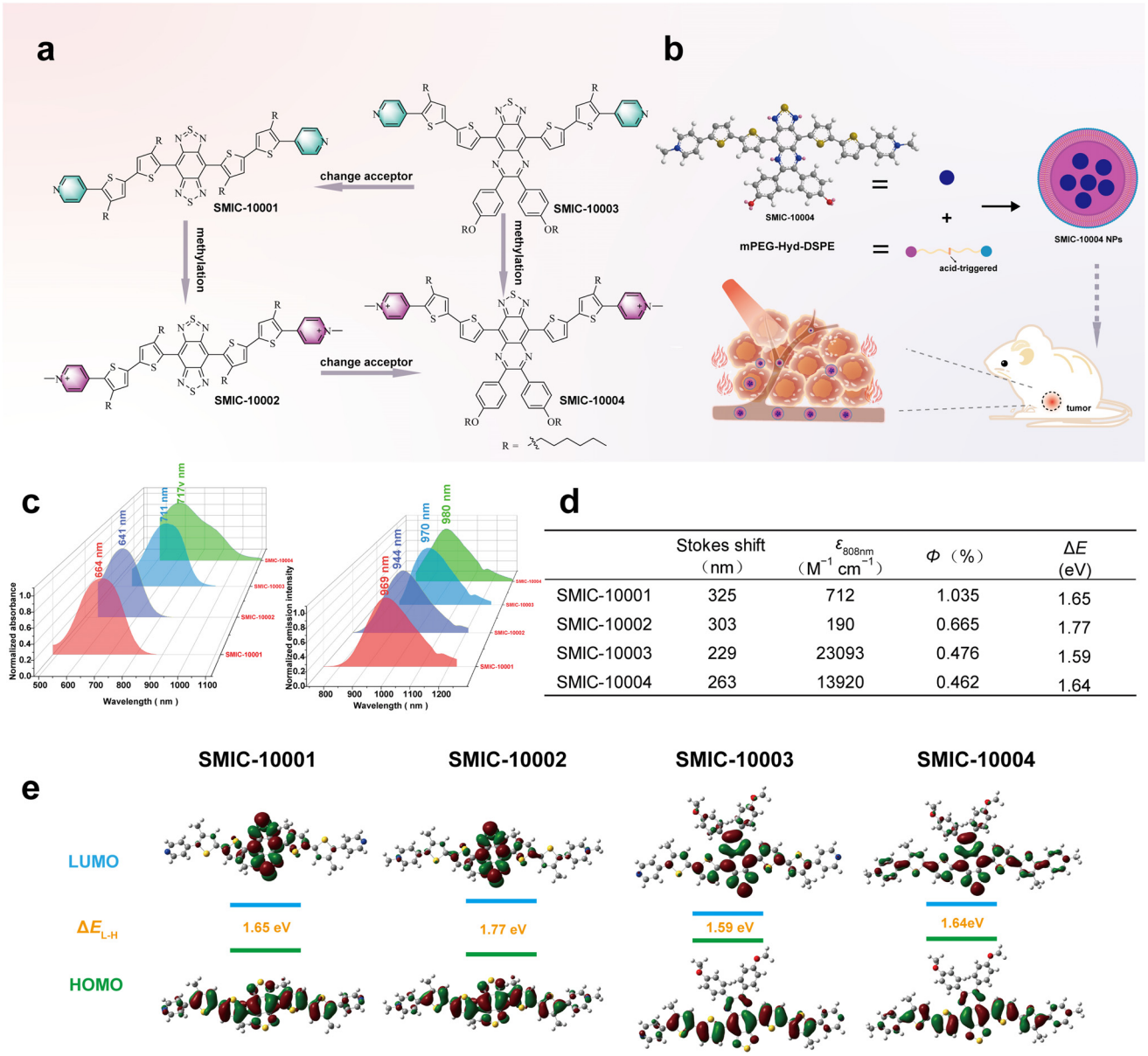

	Stokes shift (nm)	ε_{808nm} (M^{-1} cm^{-1})	Φ (%)	ΔE (eV)
SMIC-10001	325	712	1.035	1.65
SMIC-10002	303	190	0.665	1.77
SMIC-10003	229	23093	0.476	1.59
SMIC-10004	263	13920	0.462	1.64

Fig. 1 Design, optical properties, and biomedical applications of cationic D–A–D NIR-II probes. (a) Molecular design and chemical structures of cationic D–A–D-type NIR-II dyes. (b) Schematic illustration of mPEG-Hyd-DSPE encapsulated with D–A–D dyes and biomedical applications. (c) Absorption and emission spectra of the dyes in dichloromethane. (d) Summary of the photophysical properties of D–A–D dyes, including the Stokes shift, molar absorption coefficient (ε) at 808 nm, relative quantum yield (Φ), and energy gap (ΔE). (e) DFT calculations of the HOMO and LUMO distributions of the D–A–D dyes.

SMIC-10002 was soluble in methanol and remained dispersible in 1% DMSO solution. Keeping the donor segments constant, the central acceptor of SMIC-10001 was replaced with TQX, yielding SMIC-10003. Compared with SMIC-10001, this structural modification extended the π-conjugation, resulting in a red-shifted absorption of 77 nm, while the emission wavelength remained nearly unchanged, leading to a reduced Stokes shift (Fig. 1d). This observation suggests that the BBTD unit in SMIC-10001 possesses stronger electron-withdrawing capability than TQX, leading to a greater HOMO–LUMO energy gap. Following the same methylation strategy, SMIC-10004—the cationic analogue of SMIC-10003—was synthesized. Interestingly, SMIC-10004 exhibited a blue-shifted absorption peak at 717 nm but a red-shifted emission peak at 980 nm, resulting in a significantly larger Stokes shift. Methylation broadens the absorption spectrum of SMIC-10004 relative to SMIC-10003, but no such effect is observed between SMIC-10002 and SMIC-10001. It is speculated that the spectral broadening of SMIC-10004 compared with SMIC-10003 is mainly attributed to its lower solubility in DCM (all absorption spectra were recorded in DCM). The poorer solubility likely induces slight aggregation in solution, leading to the observed

broadening. In contrast, SMIC-10001 and SMIC-10002 exhibit better solubility in DCM and thus no obvious spectral broadening is observed. Additionally, SMIC-10004 demonstrated improved solubility in DMSO compared to its neutral counterpart SMIC-10003, further supporting the beneficial effect of cationic modification on polarity and solubility.

To explore the underlying photophysical mechanisms, density functional theory (DFT) calculations were performed using the B3LYP/6-31G(d) basis set combined with the SCRF solvent model. As shown in Fig. 1e, the spatial distribution and isosurface plots of the lowest unoccupied molecular orbital (LUMO) revealed that the LUMO was primarily localized on the central electron-accepting cores (BBTD or TQX). Upon extension of the conjugated system, both the LUMO and highest occupied molecular orbital (HOMO) energy levels increased, resulting in a narrowed energy gap (ΔE). In contrast, the introduction of positive charges through methylation enlarged the overall energy gap (ΔE), which corresponded well to the observed hypsochromic shift in the absorption spectra.

Fluorescence quantum yield (QY) is a key parameter in evaluating the photoluminescence efficiency of dyes. Although SMIC-10001 and SMIC-10002 exhibited absorption peaks at around 660 nm, their emission extended into the NIR-II region, making the selection of appropriate QY reference standards challenging. However, SMIC-10003 and SMIC-10004 exhibited strong absorption at 808 nm with NIR-II fluorescence emission, showing similar spectral characteristics to IR-26. Consequently, we employed the widely adopted IR-26 (QY = 0.05%) as the reference dye to determine the relative QY of SMIC-10004, which was found to be 0.462% (Fig. 1c). Although the QY under excitation at different wavelengths may vary, due to the lack of a suitable reference standard, SMIC-10004 was selected as the reference compound with an assumed QY of 0.462%. This approach enabled a qualitative comparison of the QY of the aforementioned dyes to a certain extent. The relative QY values of SMIC-10001, SMIC-10002, and SMIC-10003 were measured as 1.035%, 0.665%, and 0.476%, respectively. Interestingly, despite its more extended conjugation, the TQX-based compound exhibited a lower QY compared to its BBTD counterpart. Furthermore, across different structural frameworks, methylation consistently led to a reduction in QY, which may be attributed to the altered excited-state energy landscape resulting from the hypsochromic shift in absorption.

2.2 Synthesis and characterization of SMIC-10004 NPs

For biological imaging and therapy, a desirable probe should possess good water solubility. We initially attempted to disperse these probes in phosphate-buffered saline (PBS), but their solubility was poor, and the aqueous fluorescence was faint. Although the introduction of charges increased the polarity of the molecules to some extent, the rigid conjugated backbone and hydrophobic alkyl side chains still hindered the free dissolution in aqueous environments. Therefore, a biocompatible carrier that prevents direct contact of the small-molecule dyes with water and addresses their solubility issue was required.

Polyethylene glycol (PEG) modification is an effective strategy for improving the aqueous solubility of positively charged therapeutic agents and shielding their surface charge, thereby enhancing their biocompatibility. However, the presence of PEG may hinder cellular uptake.[32,33] To overcome this challenge, hydrazone (Hyd) offers an elegant solution: Hyd bonds remain stable at physiological pH but are readily cleaved under acidic conditions commonly found in tumor tissues or endocytic vesicles (pH $\leq$ 6).[34] Thus, PEGylated materials linked *via* Hyd bonds achieve prolonged systemic circulation while enabling pH-responsive de-shielding of PEG in acidic microenvironments,[35] thereby enhancing drug release and tumor-specific retention. We employed mPEG-Hyd-DSPE as the encapsulating material and used a self-assembly strategy to construct water-soluble fluorescent nanoprobes, successfully solving the issue of poor water solubility of the dyes. The resulting dye-loaded nanoparticles were named SMIC-10001 NPs, SMIC-10002 NPs, SMIC-10003 NPs and SMIC-10004 NPs, respectively. Their particle size measurements are shown in Fig. 2a and Fig. S15(a–c).

After encapsulation into nanoparticles, the fluorophores retained their characteristic NIR-II emission properties (Fig. S16). Compared with their unencapsulated forms, SMIC-10001 NPs and SMIC-10002 NPs exhibit red-shifted absorption and slightly blue-shifted emission peaks, while both the absorption and emission peaks of SMIC-10003 NPs and SMIC-10004 NPs show red shifts. These differences may arise from the enhanced polarity of the encapsulated environment, which stabilizes the ground state and induces red-shifted absorption. However, the alkyl substituents on the thiophene donors adjacent to the BBTD core in SMIC-10001 and SMIC-10002 introduce steric hindrance, thereby reducing effective conjugation and restricting structural relaxation in the excited state, ultimately leading to shorter emission wavelengths. By comparison, SMIC-10003 and SMIC-10004 maintain superior planarity and extended conjugation, which result in pronounced red shifts in both absorption and emission. During the encapsulation process, we observed an interesting phenomenon: under identical feeding ratio and sonication conditions, SMIC-10003 exhibited a significantly lower encapsulation efficiency. The resulting SMIC-10003 nanoparticles also showed larger hydrodynamic sizes, along with visible sedimentation of fine particles during static storage. In the post-processing steps, a large portion of oversized nanoparticles was removed by the filtration membrane, leading to substantial sample loss. Neither increasing the feeding ratio nor extending the sonication time resulted in notable improvements. In contrast, the positively charged SMIC-10004 demonstrated an encapsulation efficiency close to 100%. Repeated experiments consistently yielded nanoparticles with uniform size distribution and high colloidal stability (Fig. 2a and Fig. S15d, 17). These nanoparticles passed through filtration membranes without loss and remained stable without sedimentation over extended periods. This indicated a more con-

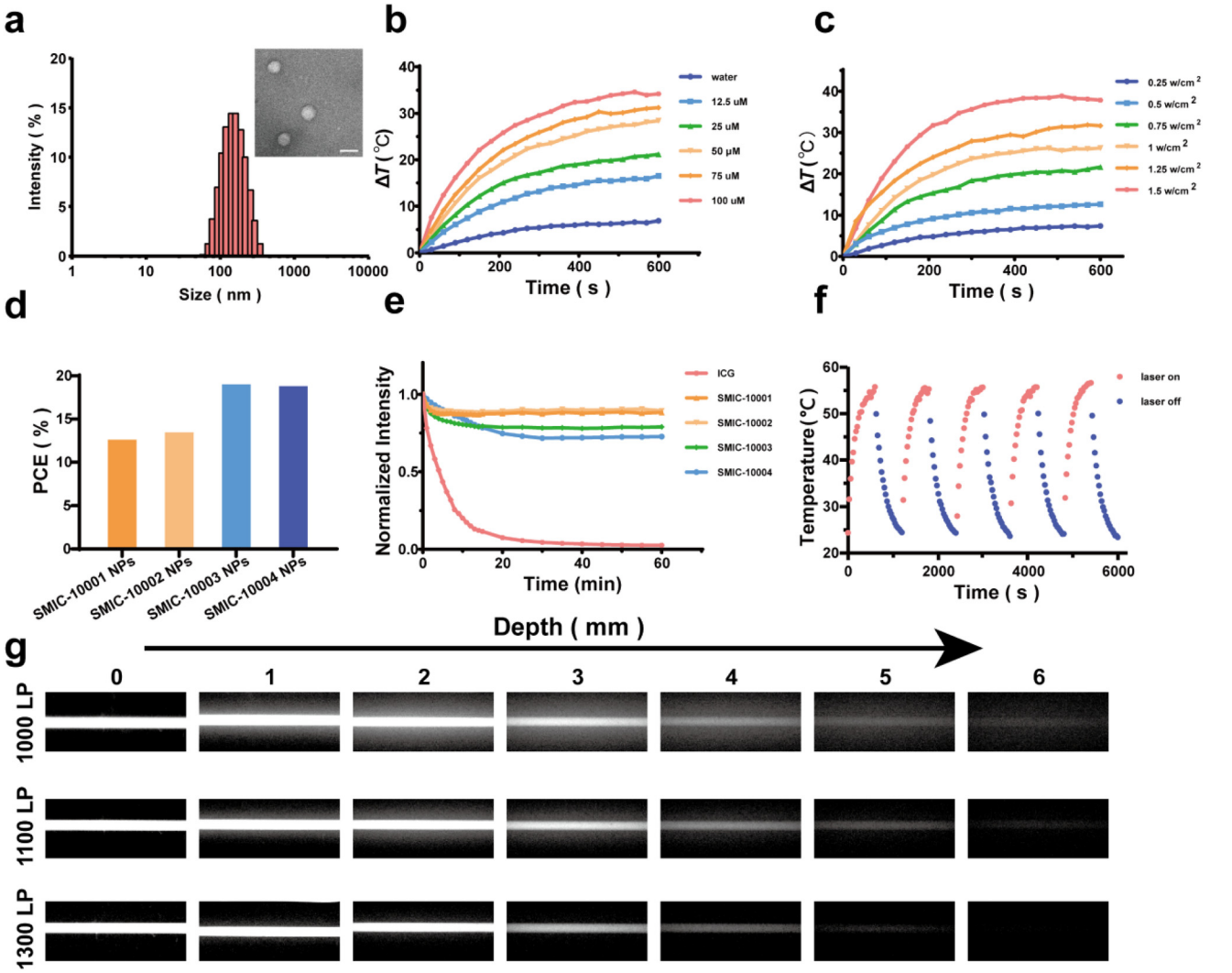

Fig. 2 Photophysical properties of D–A–D fluorescent probes. (a) Dynamic light scattering profile and transmission electron microscopy image of SMIC-10004 NPs. (b) Temperature elevation curves of SMIC-10004 NPs at different concentrations under 808 nm (1.0 W cm^{-2}) laser irradiation. (c) Temperature elevation of SMIC-10004 NPs (80 μM) at various laser power densities (808 nm). (d) Calculated photothermal conversion efficiencies of various nanoparticles. (e) Photostability comparison of SMIC-10001, SMIC-10002, SMIC-10003, SMIC-10004, and ICG under continuous 808 nm (50 mW cm^{-2}) laser irradiation for 60 minutes. (f) Photothermal stability of SMIC-10004 NPs (80 μM) over five cycles of laser on/off irradiation (808 nm, 1.0 W cm^{-2}). (g) NIR-II fluorescence images of SMIC-10004 NPs loaded in capillary tubes embedded at depths of 0–6 mm in 1% intralipid solution under 808 nm (50 mW cm^{-2}) excitation, using long-pass filters at 1000, 1100, and 1300 nm. Scale bar: 200 μm.

trollable and reproducible nanoparticle formation process. It was thus considered that the introduction of positive charges enhanced intermolecular electrostatic repulsion, thereby suppressing probe aggregation and promoting better dispersion. This likely contributes to the formation of more stable and structurally favorable nanoparticles.

To further examine the role of acid-responsiveness, SMIC-10004 was encapsulated using either mPEG-Hyd-DSPE or mPEG-DSPE, yielding SMIC-10004 NPs and SMIC-10004 NPs-N, respectively. After nanoparticle formation, both formulations maintained the NIR absorption and emission properties of the parent fluorophore. The colloidal stability of these nanoparticles was evaluated *in vitro* under different pH conditions (pH 8.0, 7.4, 6.0, and 5.5) using dynamic light scattering measurements over 24 hours. The results revealed that SMIC-10004 NPs-N remained stable, whereas SMIC-10004 NPs showed signs of partial swelling and the emergence of smaller-sized nanoparticles (Fig. S18 and 19), suggesting that the hydrazone linker effectively responded to acidic environments.

2.3 Photothermal performance of SMIC-NPs

Photothermal conversion efficiency and photothermal stability are key indicators in evaluating the performance of photothermal agents. After encapsulation into nanoparticles, the SMIC dyes exhibited good dispersibility in aqueous solution, with an average hydrodynamic diameter of 132.6 nm and a polydispersity index of 0.188 (Fig. 2a). Transmission electron microscopy images reveal that the obtained nanoparticles exhibit a

uniform spherical morphology. The temperature elevation of SMIC-10004 NPs at different concentrations (0, 12.5, 25, 50, 75, and 100 μM) was recorded under 808 nm (1.0 W cm^{-2}) laser irradiation (Fig. 2b), and the corresponding photothermal conversion efficiency was calculated (Fig. S20–23). Considering its broad NIR emission profile and stable formulation, SMIC-10004 NPs were selected for further investigation.

Moreover, by fixing the concentration and varying the laser power density (0.25, 0.5, 0.75, 1, 1.25, and 1.5 W cm^{-2}), a series of temperature curves were obtained (Fig. 2c), demonstrating a strong correlation between photothermal performance and either laser power or nanoparticle concentration. Higher laser intensity or increased NP concentration resulted in more intensive temperature elevation. The photothermal conversion efficiencies of SMIC-10001 NPs, SMIC-10002 NPs, SMIC-10003 NPs, and SMIC-10004 NPs were calculated to be 10.72%, 11.37%, 19.0%, and 18.51%, respectively (Fig. 2d). These results suggest that the TQX-based structures possess higher photothermal efficiency than their BBTD analogues, likely due to a more extended π-conjugation. In addition, the TQX core exhibits a more red-shifted fluorescence spectrum compared with BBTD, making it a more suitable candidate for photothermal agents. However, the introduction of positive charge appeared to have a negligible effect on photothermal performance. According to the vertical excitation energy (ΔE_{S0-S1}) results shown in Table S1, it can be observed that the differences after the introduction of positive charges are all less than 0.1 eV, indicating no significant changes. This suggests that the driving force for non-radiative transitions has not changed considerably, and therefore, no considerable variation in photothermal conversion efficiency is observed.

D–A–D-type molecules are generally known for their excellent photostability compared to cyanine-based dyes. Among the synthesized dyes, SMIC-10001 and SMIC-10002 exhibited strong absorption at 660 nm but relatively weak absorption at 808 nm. In contrast, SMIC-10003 and SMIC-10004 displayed strong absorption peaks at both 660 nm and 808 nm. The fluorescence intensity under both 660 nm and 808 nm excitation

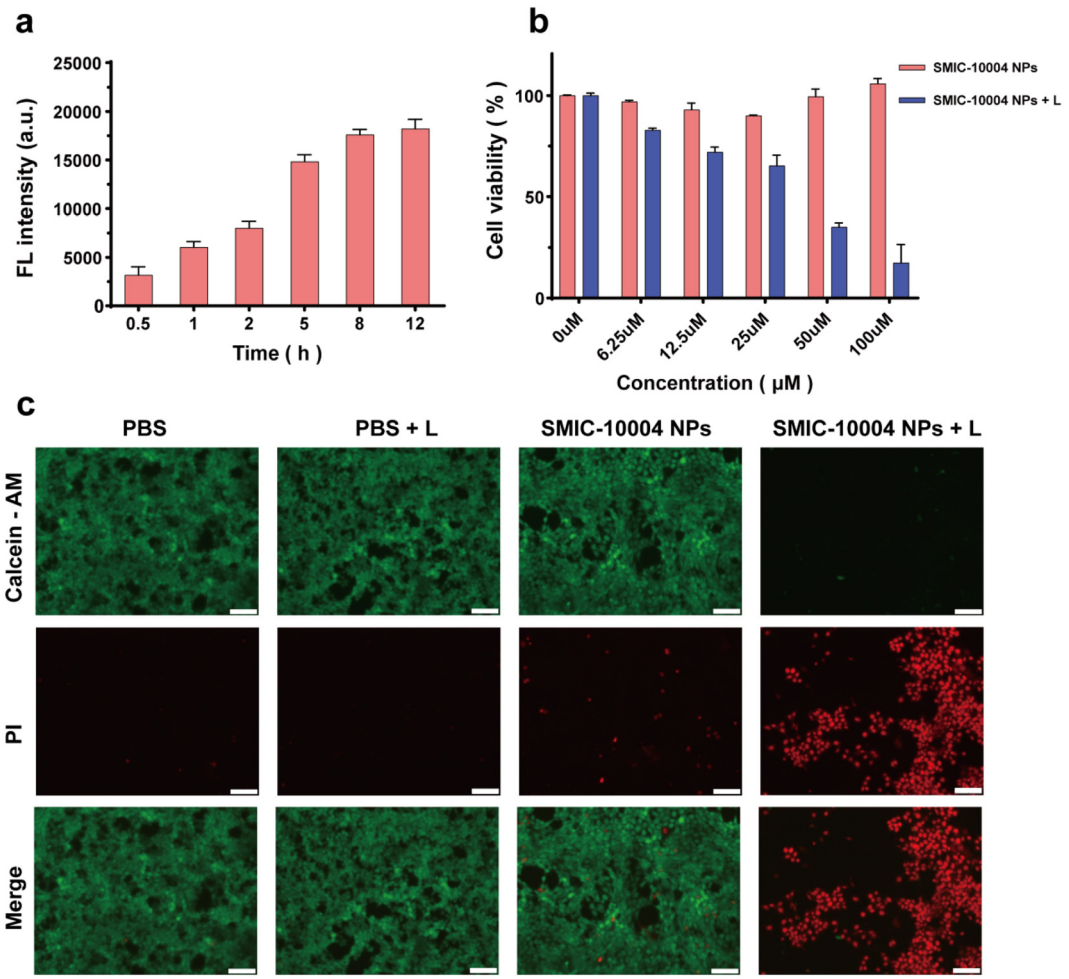

Fig. 3 *In vitro* study of cellular uptake and photothermal therapy. (a) Cellular uptake of SMIC-10004 NPs by 4T1 cells over time. (b) Cell viability of 4T1 cells treated with SMIC-10004 NPs with or without 808 nm laser irradiation (1.0 W cm^{-2}). (c) Live/dead cell staining of 4T1 cells after treatment with SMIC-10004 NPs followed by 808 nm laser irradiation (1.0 W cm^{-2}). Live cells were stained with calcein-AM (green) and dead cells were stained with propidium iodide (PI, red). Scale bar: 100 μm.

was tested to assess their photostability. Under 660 nm laser irradiation, the fluorescence intensity of ICG dropped to 25% within 55 minutes, whereas the SMIC dyes maintained nearly constant intensities (Fig. S24). Under 808 nm irradiation, ICG showed a rapid decrease in fluorescence, with complete quenching observed within 20 minutes. In contrast, SMIC dyes exhibited only a slight initial reduction followed by stable emission, indicating superior photostability (Fig. 2e). To evaluate thermal stability, five cycles of heating–cooling were conducted using SMIC-10004 NPs under 808 nm (1.0 W cm^{-2}) laser irradiation (10 minutes, followed by natural cooling to room temperature). The temperature elevation profiles remained consistent across all cycles, confirming the excellent photothermal stability of SMIC-10004 NPs (Fig. 2f).

Furthermore, to assess the imaging performance of the dye, we used lipid emulsion to simulate different tissue depths. Owing to its broad NIR emission, SMIC-10004 NPs were tested with various long-pass filters (Fig. 2g). Remarkably, even at a simulated depth of 5 mm, the fluorescence signal remained detectable with discernible edges. Additionally, the signal-to-background ratio improved with longer filter cut-off wavelengths, highlighting the great potential of SMIC-10004 NPs for high-resolution *in vivo* imaging (Fig. S25).

2.4 Cell experiment

Encouraged by the excellent photophysical properties of SMIC-10004 NPs, their *in vitro* photothermal performance was further evaluated using 4T1 breast cancer cells. First, the cellular uptake behavior was investigated by monitoring the NIR-II fluorescence intensity in 4T1 cells at different incubation times. As shown in Fig. 3a, the fluorescence signal gradually increased with prolonged incubation, indicating the successful internalization of SMIC-10004 NPs by the cells. The uptake plateaued at approximately 8 hours, suggesting a saturated accumulation within the cells.

Next, the cytotoxicity of SMIC-10004 NPs was assessed under both dark and irradiated conditions (Fig. 3b). In the absence of laser irradiation, SMIC-10004 NPs showed negligible cytotoxicity, maintaining high cell viability even at elevated concentrations. Upon exposure to an 808 nm (1.0 W cm^{-2}) laser, however, a clear decrease in cell viability was observed in the SMIC-10004 NP-treated group. The photothermal-induced cytotoxicity exhibited a concentration-dependent trend; when the concentration reached 50 μM or higher, significant cell death was recorded, confirming the potent photothermal ablation effect of SMIC-10004 NPs upon NIR irradiation.

To further visualize the photothermal therapeutic effect, a live/dead cell assay using calcein-AM and propidium iodide (PI) was performed. In the control groups (PBS, laser only, or NPs without a laser), cells predominantly emitted green fluorescence, indicating good viability. In contrast, the cells in the "SMIC-10004 NP + laser" group showed strong red fluorescence, demonstrating effective photothermal destruction (Fig. 3c). These results confirm the promising photothermal therapy (PTT) capability of SMIC-10004 NPs against cancer cells under NIR laser irradiation.

2.5 *In vivo* NIR-II imaging

Considering the excellent NIR-II optical properties of SMIC-10004 NPs, we further evaluated their *in vivo* imaging

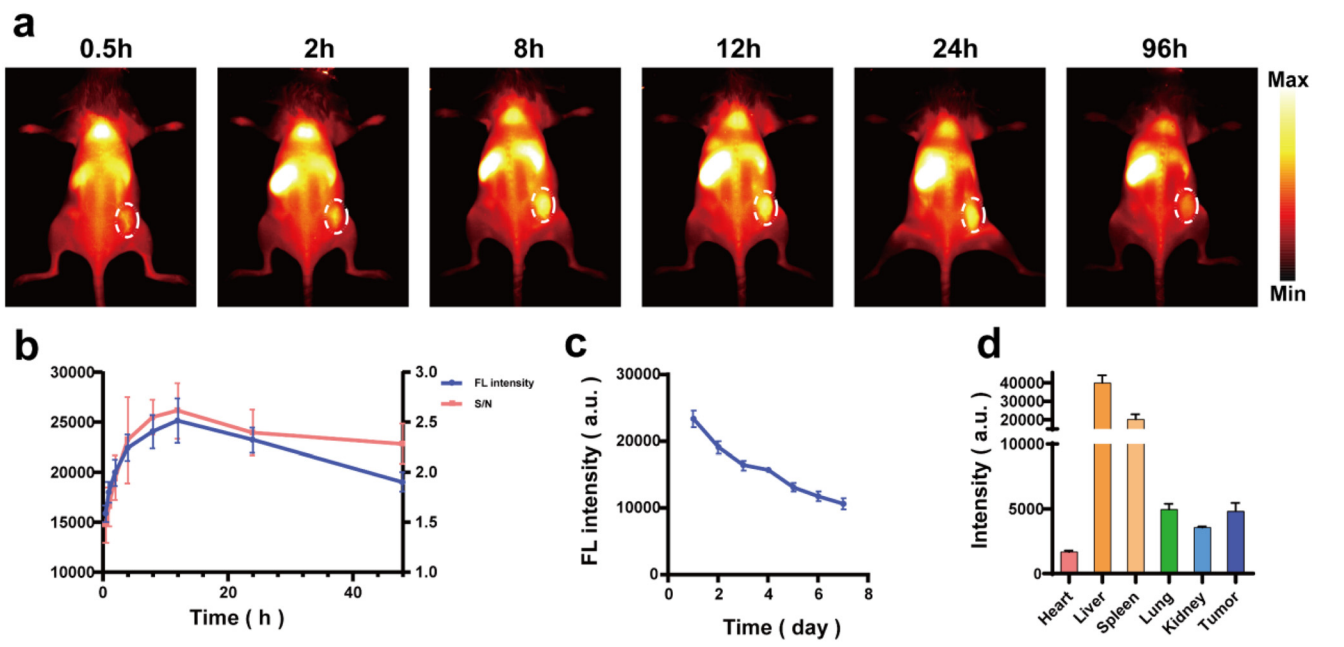

Fig. 4 *In vivo* NIR-II fluorescence imaging of SMIC-10004 NPs in 4T1 tumor-bearing Balb/c mice. (a) NIR-II fluorescence images captured at 0.5, 2, 8, 12, 24, and 96 hours post-intravenous injection of SMIC-10004 NPs. Tumor sites are highlighted with dashed circles. (b) Tumor fluorescence intensity and tumor-to-normal tissue signal ratio (T/NT) over 0–48 hours. (c) Fluorescence intensity changes at the tumor site from day 2 to day 7 post-injection. (d) *Ex vivo* fluorescence intensities of the major organs and tumors harvested at 18 hours post-injection.

performance using 4T1 tumor-bearing BALB/c mice. All animal procedures were performed under the guidelines approved by the Institutional Animal Care and Use Committee (IACUC) of the Shanghai Institute of Materia Medica, Chinese Academy of Sciences. After intravenous injection of SMIC-10004 NPs, the fluorescence intensity of the tumor gradually increased in whole-body NIR-II imaging, which could be attributed to the passive targeting capability of the nanoparticles *via* the enhanced permeability and retention (EPR) effect. A detectable fluorescence signal at the tumor appeared at approximately 0.5 h post-injection and reached its maximum intensity at around 12 h (Fig. 4a). Benefiting from the low tissue autofluorescence and high penetration depth of NIR-II imaging, SMIC-10004 NPs enabled clear visualization of tumor boundaries and high tumor-to-background contrast. Quantitative analysis revealed that the tumor-to-normal tissue (T/NT) fluorescence intensity ratio gradually increased, peaking at 2.62 at 12 h (Fig. 4b), suggesting this time point as the optimal window for therapeutic intervention. Notably, strong fluorescence signals were still observed in the tumor 96 hours post-injection and remained detectable for up to 7 days (Fig. 4c), indicating the potential of SMIC-10004 NPs for long-term imaging applications.

To investigate the biodistribution of SMIC-10004 NPs, the mice were euthanized at 18 h post-injection, and the major organs and tumors were harvested for *ex vivo* imaging (Fig. 4d). Strong fluorescence signals were observed in the liver and spleen, likely due to nanoparticle accumulation through the reticuloendothelial system, which is commonly observed for nanomaterials. At 96 h post-injection, the fluorescence signals in most organs significantly decreased, suggesting that SMIC-10004 NPs were gradually cleared *via* hepatic and splenic

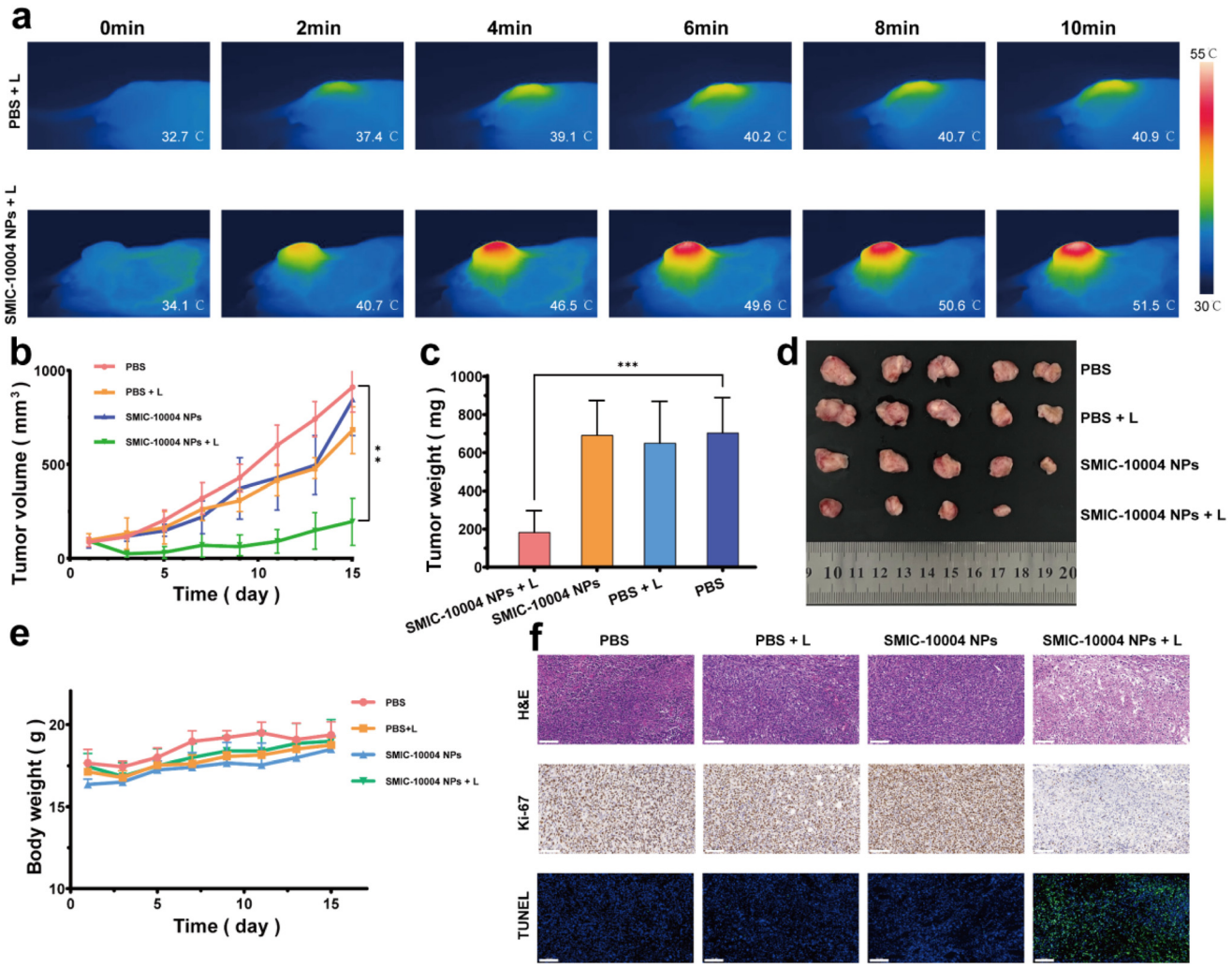

Fig. 5 *In vivo* photothermal therapy and therapeutic evaluation of SMIC-10004 NPs in 4T1 tumor-bearing mice. (a) Infrared thermal images of mice 12 hours after intravenous injection of PBS or SMIC-10004 NPs followed by 808 nm laser irradiation (1.0 W cm^{-2}, 10 min) at the tumor. (b) Tumor growth curves of mice from different treatment groups. (c) Tumor weights at the end of the treatment period. (d) Representative tumor photographs collected on day 15 post-treatment. (e) Body weight changes of mice during the treatment course. (f) Histological and immunohistochemical analyses of tumor sections by H&E staining, the TUNEL assay, and Ki-67 immunohistochemistry. Scale bar: 100 μm.

metabolic pathways. These results demonstrate that SMIC-10004 NPs possess favorable tumor-targeting capabilities and excellent NIR-II imaging properties for *in vivo* applications.

2.6 *In vivo* photothermal therapy and biosafety evaluation

To evaluate the *in vivo* photothermal therapeutic efficacy of SMIC-10004 NPs, 4T1 breast tumor-bearing Balb/c female mice were prepared as the animal model. When the tumor volume reached approximately 80 mm^3, the mice were randomly divided into four groups: (1) PBS, (2) PBS + laser (PBS + L), (3) SMIC-10004 NPs, and (4) SMIC-10004 NP + laser (SMIC-10004 NPs + L). All groups received intravenous injection *via* the tail vein. At 12 h post-injection, the tumor regions of mice in the PBS + L and SMIC-10004 NP + L groups were irradiated with an 808 nm laser (1.0 W cm^{-2}, 10 min) to initiate photothermal therapy.

Infrared thermal imaging showed that, under laser irradiation, the tumor in the SMIC-10004 NP + L group exhibited a rapid temperature increase of approximately 16 °C, significantly higher than the 8 °C rise observed in the PBS + L group (Fig. 5a). These results confirmed that SMIC-10004 NPs effectively accumulated in the tumor and converted light into heat, enabling localized and precise photothermal therapy.

Subsequently, the therapeutic efficacy was monitored for 15 days, with the tumor volume and body weight recorded every two days. As shown in (Fig. 5b), tumors in the PBS, PBS + L, and SMIC-10004 NP groups continued to grow rapidly, indicating negligible antitumor effects. In contrast, tumor growth in the SMIC-10004 NP + L group was significantly inhibited, with both the tumor volume and weight markedly reduced by the end of treatment. The tumor inhibition rate, calculated based on the excised tumor weights (Fig. 5c), reached 73.87%, demonstrating a significant antitumor effect (Fig. 5d). In addition, no significant differences in body weight were observed among the groups during the treatment period (Fig. 5e).

To further elucidate the antitumor mechanism, tumor tissues from each group were subjected to H&E staining, Ki-67 immunohistochemistry, and TUNEL apoptosis assays. The SMIC-10004 NP + L group displayed severe tissue destruction and necrosis, significantly reduced cell proliferation (Ki-67), and the highest level of TUNEL-positive apoptotic cells, confirming effective tumor ablation *via* photothermal therapy (Fig. 5f).

Additionally, potential long-term toxicity was assessed by serum biochemical analysis and H&E staining of the major organs (Fig. S26a and b). At day 7 post-injection, hepatic markers including aspartate aminotransferase (AST), alanine aminotransferase (ALT), and alkaline phosphatase (ALP) remained comparable to those in the PBS group, indicating no obvious liver damage. Renal indicators such as albumin (ALB), creatinine (CREA), and urea (UREA) were also within normal ranges, confirming minimal kidney toxicity. Leukocyte counts and the percentages of neutrophils, lymphocytes, monocytes, eosinophils, and basophils remained within normal ranges, with TNF-α at very low levels and IL-6 undetectable (Fig. S26c), reflecting the negligible immunotoxicity of SMIC-10004 NPs. *Ex vivo* fluorescence imaging of the major metabolic organs (liver, spleen, and kidneys) at 3, 7, and 14 days post-injection revealed gradual probe clearance (Fig. S26d), further demonstrating their favorable biosafety.

In summary, SMIC-10004 NPs not only offer effective NIR-II imaging capabilities, but also exhibit excellent photothermal therapeutic efficacy and biosafety *in vivo*, highlighting their potential as a promising nanoplatform for image-guided photothermal cancer therapy.

3. Conclusion

In this study, two groups of positively charged D–A–D-type small-molecule dyes were rationally designed and synthesized. The results show that introducing positive charges into the acceptor induces only slight changes in photophysical properties, such as absorption/emission spectra, QY, and photothermal conversion efficiency, without causing a significant impact. Overall, the properties remain largely consistent with those of the neutral molecules. Notably, the introduction of charges significantly increases the molecular polarity, providing valuable insights for the design of water-soluble probes. Among SMIC dyes, SMIC-10004 features an extended rigid conjugated system and cationic properties. It demonstrates stable photophysical characteristics, strong NIR-II emission, and good biocompatibility. The acid-responsive SMIC-10004 NPs integrate excellent NIR-II imaging capability and photothermal therapeutic efficacy with high biosafety. *In vivo* experiments further demonstrated that they represent a promising theranostic nanoplatform for cancer treatment. The introduction of positive charge not only provides a novel strategy for the structural optimization of D–A–D-type molecules, but also lays the foundation for the development of high-performance NIR-II photothermal therapeutic agents.

Author contributions

Shu Gao: investigation, data curation, formal analysis, visualization, writing – original draft, and writing – review & editing. Jiahui Wang: investigation. Xiaonan Wei: investigation. Jun Wang: formal analysis and visualization. Yuanpeng Jiang: resources and visualization. Boyu Tan: investigation. Yeshan Qin: methodology. Xiaoyang Zhu: investigation. Ruihu Song: investigation. Chunrong Qu: conceptualization, methodology, and supervision. Kun Qian: conceptualization, methodology, supervision, and project administration. Zhen Cheng: conceptualization, funding acquisition, supervision, and project administration. All authors have approved the final version of the manuscript.

Conflicts of interest

The authors declare that there are no conflicts of interest regarding the publication of this paper.

Data availability

The data supporting this article have been included as part of the supplementary information (SI). Supplementary information: experimental procedures; synthetic routes; NMR and MS spectra; acid-responsive behavior of nanoparticles; photothermal data analysis; penetration depth data; hematoxylin–eosin (H&E) staining. See DOI: https://doi.org/10.1039/d5bm01084e.

Acknowledgements

This work was partially supported by the National Natural Science Foundation of China under grant No. U2267221, the Strategic Priority Research Program of the Chinese Academy of Sciences (XDB0830300), and the Shandong Laboratory Program (SYS202205).

References

1 X. Liu, B. Yu, Y. Shen and H. Cong, *Coord. Chem. Rev.*, 2022, **468**, 214609.
2 Y. Chen, J. Chen and B. Chang, *iRadiology*, 2023, **1**, 36–60.
3 B. Chang, J. Chen, J. Bao, T. Sun and Z. Cheng, *Chem. Rev.*, 2023, **123**, 13966–14037.
4 S. He, J. Song, J. Qu and Z. Cheng, *Chem. Soc. Rev.*, 2018, **47**, 4258–4278.
5 K. Qian, C. Qu, X. Ma, H. Chen, M. Kandawa-Schulz, W. Song, W. Miao, Y. Wang and Z. Cheng, *Chem. Commun.*, 2020, **56**, 523–526.
6 J. Guo, M. Du, Z. Chen, X. Chen and Z. Yuan, *iRadiology*, 2023, **1**, 209–224.
7 T. Li, C. Li, Z. Ruan, P. Xu, X. Yang, P. Yuan, Q. Wang and L. Yan, *ACS Nano*, 2019, **13**, 3691–3702.
8 Z. Zhang, Y. Du, X. Shi, K. Wang, Q. Qu, Q. Liang, X. Ma, K. He, C. Chi, J. Tang, B. Liu, J. Ji, J. Wang, J. Dong, Z. Hu and J. Tian, *Nat. Rev. Clin. Oncol.*, 2024, **21**, 449–467.
9 J. Liu, H. Chen, Y. Yang, Q. Wang, S. Zhang, B. Zhao, Z. Li, G. Yang and G. Deng, *Mater. Horiz.*, 2023, **10**, 3791–3796.
10 L. Li, J. Li, X. Huang, F. Yang, J. Wang, L. Zhao, J. Liu and G. Deng, *Sens. Actuators, B*, 2025, **443**, 138295.
11 H. Chen, S. Yan, L. Zhang, B. Zhao, C. Zhu, G. Deng and J. Liu, *Sens. Actuators, B*, 2024, **405**, 135346.
12 X. Zhao, F. Zhang and Z. Lei, *Chem. Sci.*, 2022, **13**, 11280–11293.
13 R. Song, Y. Dong, Z. Zhong, Q. Zhao, Y. Hu, M. Lei, P. Lei, Z. Jiang, K. Qian, C. Shi, Z. He, Y. Qin, J. Wang and H. Chen, *J. Med. Chem.*, 2024, **67**, 10275–10292.
14 J. Mu, M. Xiao, Y. Shi, X. Geng, H. Li, Y. Yin and X. Chen, *Angew. Chem., Int. Ed.*, 2022, **61**, e202114722.
15 T. Yuan, Q. Xia, Z. Wang, X. Li, H. Lin, J. Mei, J. Qian and J. Hua, *ACS Appl. Mater. Interfaces*, 2024, **16**, 4478–4492.
16 L. Wang, N. Li, W. Wang, A. Mei, J. Shao, W. Wang and X. Dong, *ACS Nano*, 2024, **18**, 4683–4703.
17 Q. Yang, H. Ma, Y. Liang and H. Dai, *Acc. Mater. Res.*, 2021, **2**, 170–183.
18 A. L. Antaris, H. Chen, K. Cheng, Y. Sun, G. Hong, C. Qu, S. Diao, Z. Deng, X. Hu, B. Zhang, X. Zhang, O. K. Yaghi, Z. R. Alamparambil, X. Hong, Z. Cheng and H. Dai, *Nat. Mater.*, 2015, **15**, 235–242.
19 Y. Chen, H. Yu, Y. Wang, P. Sun, Q. Fan and M. Ji, *Biomater. Sci.*, 2022, **10**, 2772–2788.
20 Y. Zhong, J. Gu, Y. Su, L. Zhao, Y. Zhou and J. Peng, *Chem. Eng. J.*, 2022, **433**, 133263.
21 F. Chu, B. Feng, Y. Zhou, M. Liu, H. Zhang, M. Liu, Q. Chen, S. Zhang, Y. Ma, J. Dong, F. Chen and W. Zeng, *Chem. Sci.*, 2025, **16**, 4490–4500.
22 J. He, S. Hua, D. Zhang, K. Wang, X. Chen and M. Zhou, *Adv. Funct. Mater.*, 2022, **32**, 2208028.
23 Q. Wang, X. Zhang, Y. Tang, Y. Xiong, X. Wang, C. Li, T. Xiao, F. Lu and M. Xu, *Pharmaceutics*, 2023, **15**, 2027.
24 Y. Tang, J. Feng, S. Li, G. Yang, Z. Tao, T. Xiao, F. Lu, B. Xie, Q. Fan and Q. Wang, *J. Mater. Sci. Technol.*, 2025, **213**, 196–212.
25 Q. Wang, J. Liu, X. Zhang, Y. Tang, Y. Xiong, L. Zhang, T. Xiao and Q. Fan, *Chem. Commun.*, 2023, **59**, 9611–9614.
26 J. Liu, X. Zhang, M. Fu, X. Wang, Y. Gao, X. Xu, T. Xiao, Q. Wang and Q. Fan, *Biomater. Sci.*, 2023, **11**, 7124–7131.
27 S. Ning, P. Shangguan, X. Zhu, X. Ou, K. Wang, M. Suo, H. Shen, X. Lu, X. Wei, T. Zhang, X. Chen and B. Z. Tang, *J. Am. Chem. Soc.*, 2025, **147**, 7433–7444.
28 C. Qu, Y. Xiao, H. Zhou, B. Ding, A. Li, J. Lin, X. Zeng, H. Chen, K. Qian, X. Zhang, W. Fang, J. Wu, Z. Deng, Z. Cheng and X. Hong, *Adv. Opt. Mater.*, 2019, **7**, 1900229.
29 M. P. Murphy, *Biochim. Biophys. Acta*, 2008, **1777**, 1028–1031.
30 S. Gao, C. Qu, J. Wang, K. Qian and Z. Cheng, *Nano Today*, 2024, **59**, 102478.
31 K. Qian, S. Gao, Z. Jiang, Q. Ding and Z. Cheng, *Exploration*, 2024, **4**, 20230063.
32 H. Hatakeyama, H. Akita, E. Ito, Y. Hayashi, M. Oishi, Y. Nagasaki, R. Danev, K. Nagayama, N. Kaji, H. Kikuchi, Y. Baba and H. Harashima, *Biomaterials*, 2011, **32**, 4306–4316.
33 L. Mei, L. Fu, K. Shi, Q. Zhang, Y. Liu, J. Tang, H. Gao, Z. Zhang and Q. He, *Int. J. Pharm.*, 2014, **468**, 26–38.
34 L. Zhu and V. P. Torchilin, *Integr. Biol.*, 2013, **5**, 96–107.
35 Q. Sun, Z. Zhou, N. Qiu and Y. Shen, *Adv. Mater.*, 2017, **29**, 1606628.